Mapping metabolic aging and disease-associated acceleration using an interpretable NMR-based clock

Alain Ibañez de Opakua[1], Maider Bizkarguenaga[2], Ángela de Diego[2], Ricardo Conde[2], Beatriz González-Valle[2], Rubén Gil-Redondo[2], Thyerre Santana[3], Maria Luisa Seco[4], Ana Cenarro[5,6,7], Virginia Lope[6,8], Sara Margarita M. Sc.[9], Serena Pelusi M. Sc.[9], Hansjörg Habisch[10], Christoph Haudum[11], Nicolas Verheyen[12], Barbara Obermayer-Pietsch[11], Maria Pilar Sorando-Fernandez[13], Eunate Arana-Arri[14], Susana Meijide[14], Ane Miren Salazar[15], Gonzalo Hernandez[15], Montse Baldán-Martín[16,6], Paula J. Martínez-González[16,6], Fabio Suárez-Trujillo[16,6], Julia Audije-Gil[17], Juan Ignacio Arriaga[18], Milagros Iriberri[19], Miguel Ángel Moran[20,21], Xabier Camino[22], Asun Gracia[23], Ganeko Bernardo-Seisdedos[24], Adriana Sousa[25], Nádia Oliveira[25], Ignacio Verde[25], María José Zaro Bastanzuri[26], María Reyes González Fernández[27], Daniel Fernández-Bergés[26], Laura Navarrete-Arias[28], Mar Llamas-Velasco[28], Umberto Biccari[29], Roberto Morales[29], Tobias Madl[10,30], Miguel Unda-Urzaiz[6,31,32], Arkaitz Carracedo[6,31,33,34,35], Tammo Diercks[35], Adela Castelló[6,8], Hartmut Schäfer[36], Manfred Spraul[36], Claire Cannet[36], Ljubica Tasic[3], Rosario Sanchez-Pernaute[37,33], Elissabetta Buguianessi[38], Quentin Anstee[39,40], Nieves Embade[2], Shelly C. Lu[41], Francisco Mera[42], Luca Valenti[9,43], Claudo Luchinat[44,45], Danay Cibrián[28], Hortensia de la Fuente[28], Fernando Civeira[5,6,46], Dolores Arenas[17], Javier P. Gisbert[16,6], María Chaparro[16,6], Guro Giskeodegard[47], Tone Bathen[47], Enrique Zuazua[29,48,49], José M. Mato[2,6] and Oscar Millet[1,2,6,*]

[1]ATLAS Molecular Pharma, 49160 Derio, Bizkaia, Spain.
[2]Precision Medicine and Metabolism Laboratory, CIC bioGUNE, BRTA, 48160 Derio, Bizkaia, Spain.
[3]State University of Campinas (UNICAMP), 6154 Campinas, Brazil.
[4]OSARTEN Kooperativa Elkartea, 20500 Arrasate-Mondragón, Spain.
[5]Instituto de Investigación Sanitaria Aragón (IIS Aragón), Hospital Universitario Miguel Servet, 50009 Zaragoza, Spain.
[6]Consortium for Biomedical Research (CIBERCV, CIBERESP, CIBEREHD or CIBEROBN), Instituto de Salud Carlos III, Madrid, Spain.
[7]Instituto Aragonés de Ciencias de la Salud (IACS), Zaragoza, Spain.
[8]Cancer and Environmental Epidemiology Unit, Department of Epidemiology of Chronic Diseases, National Center for Epidemiology, Instituto de Salud Carlos III (ISCIII) Madrid, Spain.
[9]Precision Medicine Lab, Fondazione IRCCS Ca' Granda Ospedale Maggiore Policlinico Milano, 20122 Milano, Italy.
[10]Otto Loewi Research Center, Division of Medicinal Chemistry, Medical University of Graz, 8010 Graz, Austria.
[11]Department of Internal Medicine, Division of Medical University of Graz, 8036 Graz, Austria.
[12]Department of Internal Medicine, Division of Cardiology, Medical University of Graz, 8036 Graz, Austria.
[13]Hospital Santa Marina, Osakdietza, Biobizkaia HRI, 48004 Bilbao, Spain.
[14]Scientific Coordination, Osakidetza, Biobizkaia HRI, 48903 Barakaldo, Spain.
[15]ESAME Biomedical, Avenida Zugatzarte 8 Planta 1ª, 5; 48930 Getxo, Spain.
[16]Gastroenterology Unit, Hospital Universitario de La Princesa, Instituto de Investigación Sanitaria Princesa (IIS-Princesa), Universidad Autónoma de Madrid (UAM), and Centro de Investigación Biomédica en Red de Enfermedades Hepáticas y Digestivas (CIBEREHD), Madrid, Spain.
[17]Unidad de Investigación de la Fundación Renal Española, José Abascal 42, 28003, Madrid, Spain.
[18]Pneumology Department, Hospital Universitario de Basurto, 48013 Bilbao, Spain.
[19]Pneumology Department, Hospital Universitario de Cruces, 48903 Barakaldo, Spain.
[20]Bioaraba Health Research Institute, 01009 Vitoria-Gasteiz, Spain.
[21]Internal Medicine Department, Osakidetza, Araba University Hospital, 01009 Vitoria-Gasteiz, Spain.
[22]Hospital Universitario Donostia, 20014 San Sebastián, Spain.
[23]Sociedad Española de Médicos Generales y de Familia (SEGM), 28005 Madrid, Spain.
[24]Department of Medicine, Faculty of Health Sciences, University of Deusto, 48007 Bilbao, Spain.
[25]RISE-Health and Health Sciences Research Centre, Faculty of Health Sciences, University of Beira Interior (UBI), 6200-506 Covilhã, Portugal.
[26]Hospital Don Benito Villanueva, 06400 Badajoz, Spain.
[27]Hospital Universitario de Badajoz, 06080 Badajoz, Spain.
[28]Instituto de Investigación Sanitaria Princesa (IIS-Princesa), 28006 Madrid, Spain.
[29]Chair of Computational Mathematics, DeustoTech, University of Deusto, 48007 Bilbao, Spain.
[30]BioTechMed-Graz, 8010 Graz, Austria.
[31]Traslational prostate cancer Research lab, CIC bioGUNE-Basurto, Biocruces Bizkaia Health Research Institute, 48903 Barakaldo, Spain.
[32]Department of Urology, Basurto University Hospital, 48013Bilbao, Spain.
[33]Ikerbasque, Basque Foundation for Science, Bilbao 48011, Spain.
[34]Biochemistry and Molecular Biology Department, University of the Basque Country (UPV/EHU), 20018 Bilbao, Spain.
[35]CIC bioGUNE, BRTA, 48160 Derio, Spain.
[36]Bruker Biospin GmbH, Rudolf-Plank-Str. 23, 76275 Ettlingen, Germany.
[37]Biocruces Bizkaia Health Research Institute, 48903 Barakaldo, Spain.
[38]Gastroenterology Department, University of Turin, 10124 Turin, Italy.
[39]Translational & Clinical Research Institute, Faculty of Medical Sciences, Newcastle University, NE1 7RU Newcastle upon Tyne, UK.
[40]Newcastle NIHR Biomedical Research Centre, Newcastle Upon Tyne Hospitals NHS Trust, Newcastle upon Tyne, UK.
[41]Karsh Division of Gastroenterology and Hepatology, Cedars-Sinai Medical Center, Los Angeles, CA 90048, USA.

[42]Long COVID and Post-Viral Syndromes Unit. Bluehealthcare Clinic, 28036 Madrid, Spain.
[43]Department of Pathophysiology and Transplantation, Università degli Studi di Milano, 20122 Milano.
[44]Department of Chemistry, "Ugo Schiff", University of Florence, 50019 Sesto Fiorentino, Florence, Italy.
[45]Consorzio Interuniversitario Risonanze Magnetiche di Metallo Proteine (CIRMMP), 50019 Sesto Fiorentino, Florence, Italy.
[46]Departamento de Medicina, Psiquiatría y Dermatología, Facultad de Medicina, Universidad de Zaragoza, 50009 Zaragoza, Spain.
[47]Faculty of Medicine and Health Sciences, Northern University of Science and Technology, 7034 Trondheim, Norway.
[48]Chair for dynamics, control, machine learning, and numerics (Alexander Von Humboldt-Professorship), Department of Mathematics, Friedrich-Alexander-Universität Erlangen-Nürnberg, 91058 Erlangen, Germany.
[49]Universidad Autónoma de Madrid, Departamento de Matemáticas, 28049 Madrid, Spain

Biological age captures cumulative physiological decline but remains challenging to quantify across the full adult lifespan with mechanistic and clinical interpretability. Here we develop an interpretable metabolic aging clock based on high-throughput serum nuclear magnetic resonance (NMR) profiling in 29,390 individuals aged 7–106 years across multiple cohorts. Using a machine-learning framework that integrates quantified metabolites and NMR-inferred clinical biomarkers, we achieve accurate age prediction ($r = 0.88$; RMSE ≈ 8.7 years) while resolving the multicollinearity that limits interpretability in spectral models. Feature attribution reveals a consistent biological signature dominated by chronic inflammation, kidney function, and energy metabolism, with albumin and erythrocyte sedimentation rate emerging as principal determinants of metabolic aging. Application to eleven pathogenic cohorts (analyzing serum from 3,882 additional patient donors that represent distinctive and most frequent causes of disease), shows that metabolic age acceleration reflects disease-specific distortions rather than uniform aging shifts, where acute inflammatory states, metabolic dysfunction, and organ-specific pathologies exhibit distinct signatures. In a prospective cardiovascular cohort, metabolic age acceleration precedes clinical events, highlighting its potential for early risk stratification. Together, these results establish an interpretable, scalable metabolic clock that links systemic biochemical states to aging trajectories and disease risk and provide a framework for precision medicine applications.

Biological age, unlike chronological age, reflects the cumulative physiological decline driven by intrinsic genetic factors and extrinsic influences such as lifestyle, environment, and disease burden[1,2]. Metabolic aging clocks are computational models designed to estimate an individual's biological age by analyzing age-dependent patterns in metabolites[3,4]. Because metabolites represent the end products and intermediates of metabolic pathways, they provide an integrated and dynamic snapshot of cellular activity, mitochondrial function, and systemic homeostasis, all of which undergo progressive changes with aging[5,6].

The development of metabolic clocks builds on the observation that concentrations and interrelationships among circulating metabolites shift predictably with age across populations. Deviations between metabolic and chronological age (commonly termed "age acceleration" or "age deceleration") may signal elevated disease risk, accelerated physiological decline, or conversely, metabolic resilience[7,8]. These conceptual foundations parallel those established for epigenetic, transcriptomic, and proteomic aging clocks, but with the advantage that metabolomic data can be obtained and analyzed more readily and reflect both long-term biological processes and short-term physiological adaptations[9].

Current metabolic aging clocks employ a variety of analytical platforms, most prominently mass-spectrometry-based metabolomics and large-scale serum nuclear magnetic resonance (NMR) profiling. NMR spectroscopy has emerged as a particularly attractive platform for constructing aging clocks due to its high reproducibility, minimal sample preparation, direct quantifiability, and suitability for large-scale clinical or epidemiological studies. Furthermore, serum and plasma NMR provide unique access to clinically relevant features, such as

detailed lipoprotein subclass distributions and inflammatory glycoprotein markers (e.g., GlycA, GlycB), that are tightly linked to aging biology and cardiometabolic risk[10,11].

Several NMR-based metabolic clocks have already been developed, providing an expanding methodological foundation. Early efforts used NMR urine spectra to model metabolic age, demonstrating feasibility but limited precision due to the high short-term variability of urinary metabolites[12]. Subsequent large-scale studies leveraging serum or plasma NMR profiling have substantially improved performance: analyses of tens of thousands of individuals across Estonian, Finnish, and Dutch cohorts have shown that NMR-derived biomarker patterns can predict chronological age and associate metabolic age acceleration with all-cause mortality[7,8,13], but these studies face cohort-specific biases and limited external validity. The UK Biobank cohort has also been extensively used to develop metabolic clocks using conventional algorithms[14] and machine learning techniques[15], but over a limited age range (40-71 y.o.). In turn, prospective analyses have been conducted on the same cohort to evaluate the sensitivity of metabolomic profiles in predicting the risk of up to 50 chronic diseases[16]. Despite these advances, published NMR-based aging models suffer from regression to the mean, systematically overestimating the age of younger individuals and underestimating it in older subjects, which severely limits their performance at the extremes of the lifespan. Moreover, epidemiological studies suggest that NMR spectra may also capture information related to clinical parameters[17–19], but this possibility has not been explored in the development of metabolic clocks so far.

To address the problem of lifespan coverage in metabolic clocks and expand the clinical interpretability of the models, we assembled one large cohort of 29,390 individuals, covering a broad age range (7-106 years) with focus on adults, by combining multiple independent cohorts. In addition to the general population cohort, this resource incorporates patient groups totaling 3,882 donors and covering 11 diseases that include major non-communicable conditions as well as several infectious diseases. Building on the methodological perspective and initial proof-of-concept established in earlier NMR-based metabolomic aging research[20], we here developed a machine-learning model for age prediction that prioritizes interpretability while considering both quantified metabolite concentrations and additional clinical parameters inferred from the same NMR spectra. The objective was twofold: i) to characterize metabolic and clinical patterns that define aging trajectories within a large cohort covering the entire adult lifespan; and ii) to examine how different disease cohorts of similar geographic origin and ethnicity localize within this metabolic aging space.

Results

Cohort Assembly and NMR Spectral Acquisition

To develop metabolic aging clocks, we assembled a large cohort of 29,390 individuals by integrating up to seven different studies. The cohort was designed to represent the general population, with balanced sex distribution and a wide age range (7-106 years) but mainly targeting adult population. To independently validate the model, we also incorporated an external cohort obtained and measured in a different country and laboratory (Graz, Austria, n = 121). In addition, we included several disease-specific cohorts covering major non-communicable diseases (chronic kidney disease (CKD, n = 828), prostate cancer (PRC, n = 717), metabolic syndrome (MetS, n = 660), MASLD (n = 160), inflammatory bowel disease (IBD, n = 310), psoriasis (PSO, ns = 226), cardiovascular disease with associated posterior event (CVD, n = 59) and amyotrophic lateral sclerosis (ALS, n = 63)) as well as infectious diseases and related syndromes, including influenza (FLU, n = 158), COVID-19 (COV, n = 470), and long COVID (LCOV, n = 231). Comprehensive descriptions of the study cohorts can be found in the supplementary cohort description file (SupCoDe.pdf). Additionally, the general characteristics for each individual cohort are detailed in Extended Data Tables 1-20.

For each cohort (model training and validation, n = 29,390; external validation, n = 121; disease groups, n = 3,882), serum samples were analyzed using NMR spectroscopy. Multiple spectra were acquired (see Methods),

each optimized for sensitivity to specific molecular features, including inflammatory markers, lipoproteins, and circulating metabolites (Fig. 1).

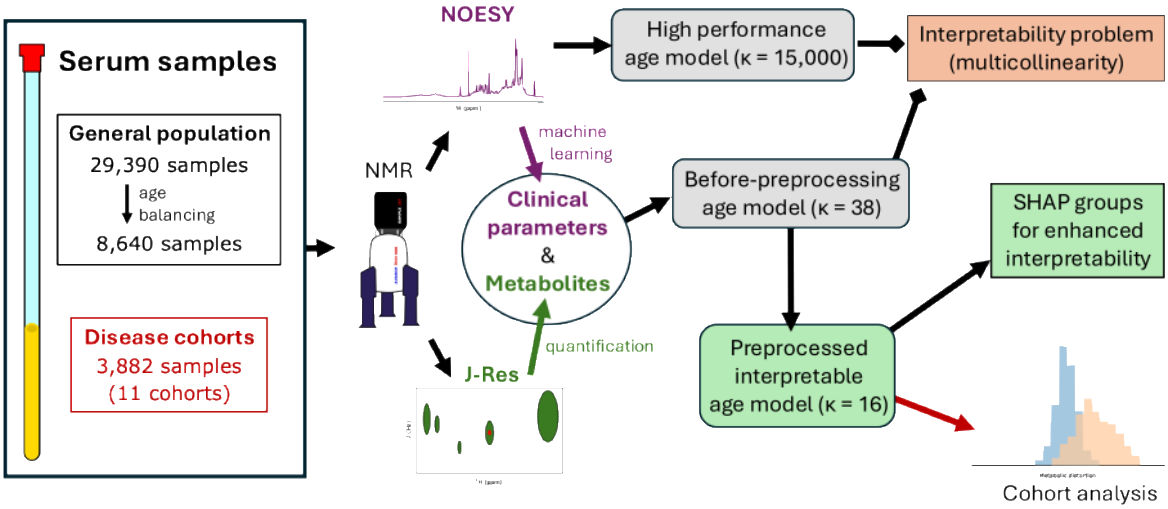

Fig. 1 | Methodological workflow for the development of the interpretable metabolic aging clock. The flowchart illustrates the study design, starting with serum samples from a general population (balanced by age) and eleven disease cohorts. NMR spectroscopy is performed to acquire NOESY and J-Res spectra. The NOESY data is used to predict clinical parameters and to build a high-performance age model; however, this age spectral model suffers from an interpretability problem due to high multicollinearity (κ=15,000). J-Res spectra are utilized for metabolite quantification. These metabolites and clinical parameters are combined into a preliminary age model, which is also limited by interpretability issues linked to multicollinearity (κ=38). To resolve this, a preprocessing step refines the features into a final interpretable age model (κ=16). Finally, SHAP groups are applied for enhanced interpretability, enabling metabolic distortion analysis in disease cohorts.

NMR signal–based models for metabolic age prediction

We first developed an age-prediction model using the binned 1D NOESY dataset, which captures signals from all molecular components detectable by NMR. To that end, we refined the full set of 29,390 samples to derive an *age-balanced* subset of 8,640 individuals (Fig. 1). The NOESY-based model achieved high predictive accuracy, with a Pearson correlation of r = 0.93 and a Root Mean Square Error (RMSE) of 6.5 years on the independent test set (Extended Data Fig. 1a).[15]

To assess whether age-associated information was specific to the NOESY acquisition, we evaluated two complementary models based on the CPMG spectrum and the NOESY information in the time domain (free-induction decay, FID). The CPMG-based model achieved a predictive performance comparable to NOESY (r = 0.92; RMSE = 6.8 years; Extended Data Fig. 1b), consistent with recent analyses demonstrating that NOESY and CPMG spectra encode highly overlapping structural variations, to the extent that CPMG profiles can be accurately derived directly from NOESY acquisitions[21]. Interestingly, the model trained on the unstructured FID data also remained highly predictive (r = 0.89; RMSE = 8.6 years; Extended Data Fig. 1c). This indicates that the dominant signals shaping the initial FID profile provide sufficient independent features for accurate age prediction without the need for a Fourier transform or accounting for the data's intrinsic time-domain sequentiality.

SHapley Additive exPlanations (SHAP) were used to interpret the model. SHAP values represent the fair, weighted average contribution of a feature across all possible combinations. When applied to the NOESY dataset, the feature contributions exhibited a characteristically broad and non-specific distribution of SHAP values (Extended Data Fig. 2a). Direct interpretation of the NOESY model in the metabolic space proved unreliable due to the extreme multicollinearity inherent to binned NMR spectra: adjacent and partially overlapping resonances produced large blocks of highly correlated bins. To robustly quantify this redundancy, we computed the condition number (κ) of the feature matrix, a metric that reflects how multicollinearity affects the overall numerical stability of the dataset. Binned NOESY data yielded $\kappa \approx 1.5 \times 10^4$, far exceeding the commonly accepted threshold of $\kappa = 30$, which indicates problematic multicollinearity[22].

Interpretable aging clocks based on NMR-derived biomarkers

The conventional approach to extract clinical value from serum NMR spectra involves assigning spectral signals to specific metabolites and quantifying them[23–26]. However, epidemiological studies based on NMR data suggest that these spectra may also capture information related to other well-established clinical parameters (directly or indirectly)[17–19]. Building on this premise, we trained supervised regression models to quantify 49 metabolites and infer 25 routinely measured clinical biomarkers, directly from NOESY spectra (see Methods and Extended Data Table 21). The selected parameters span key physiological domains, including carbohydrate and amino acid metabolism, ketone bodies, TCA cycle intermediates, and one-carbon metabolism, as well as lipid profiles, inflammatory markers, renal function indices, hematological variables, and protein-related measures. For metabolite quantification, a dedicated pipeline was applied to J-res spectra, using targeted spiking experiments as the primary validation reference. The predicted biomarkers exhibited moderate to strong correlations with their corresponding laboratory measurements (Extended Data Fig. 3), supporting their use as semiquantitative proxies rather than precise clinical measurements.

This combined feature set (74 variables in total) served as the foundation for constructing an initial interpretable metabolic age model. Although this model achieved good predictive performance ($r = 0.89$; RMSE = 8.6 years; Extended Data Fig. 4a), analysis of the feature matrix still revealed clear signs of multicollinearity, yielding a condition number of $\kappa \approx 38$ (well above the conventional threshold of 30). This redundancy structurally dispersed the resulting SHAP values, thereby compromising a clear and robust biological interpretation (Extended Data Fig. 4b)[26]. For example, GlycA and GlycB both exhibited high SHAP importance but with opposite directional effects on predicted age, a pattern that is physiologically implausible. For comparison, models trained exclusively on IVDr automated metabolite and lipoprotein reports (143 parameters)[27] also demonstrated robust predictive capacity ($r = 0.86$; RMSE = 9.3 years), but showing high collinearity ($\kappa \approx 180$) due to the lipoprotein subfraction intrinsic cross-correlation, which also introduced additional complexity in feature attribution.

To address this issue and obtain a fully interpretable biochemical representation, we intentionally bypassed automated dimensionality reduction techniques in favor of a manual, expert-curated preprocessing strategy. Starting from the original 74 features, redundant variables (exhibiting strong inter-correlations) were removed, and certain biochemical parameters were manually reformulated or aggregated to reduce overlap and improve the separability of physiologically distinct signals, resulting in a final set of 75 variables. Accordingly, hemoglobin, fructosamine, and total cholesterol were discarded due to redundancy with other biomarkers. The GlycB/GlycA ratio was computed and Glyc B removed because of its strong correlation with Glyc A. Additional metabolically meaningful ratios (including urea/creatinine, BCAA/AAA, lactate/pyruvate, and glutamine/glutamate) were introduced as potentially informative composite indicators of metabolic balance. Total protein was also decomposed into a non-albumin fraction to isolate a more specific signal. With this representation, we substantially reduced multicollinearity (from $\kappa \approx 38$ to $\kappa \approx 16$), while preserving the original biochemical meaning, thereby yielding a well-conditioned structure suitable for stable interpretation.

The interpretable model achieved high predictive performance ($r = 0.88$; RMSE = 8.7 years; Fig. 2a), notably mitigating the regression to the mean effect typically observed in published clocks. Furthermore, it approached the accuracy of the NOESY-based model despite relying on substantially fewer and more biologically constrained features. Importantly, the reduction in multicollinearity resulted in stable and coherent SHAP value distributions (Fig. 2b), in contrast to the diffuse or contradictory attribution patterns observed in the unprocessed biomarker model (Extended Data Fig. 4c).

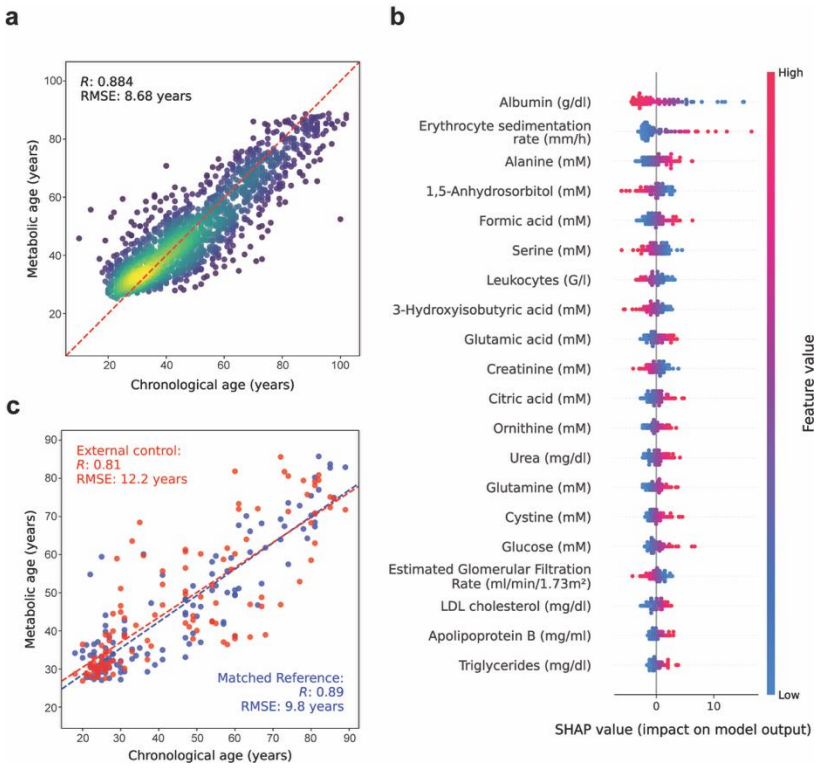

Fig. 2 | Biomarker-based interpretable metabolic age prediction model. a, Pearson correlation plot for the preprocessed biomarker feature set. The diagonal line represents the identity line, illustrating the minimal regression to the mean. **b,** SHAP summary plot for the interpretable model. Each point corresponds to one sample, positioned along the x-axis by its SHAP value for a given feature; features are ordered by mean absolute SHAP value. Point color indicates the feature value (blue = low, red = high). **c,** External validation of the model showing chronological versus metabolic age. The external control cohort (Austria) is shown in red, plotted alongside an age-matched reference dataset in blue.

To rigorously validate that the calculated metabolic distortion is not a statistical artifact driven by differences in chronological age distributions, we implemented an iterative random sub-sampling approach by using the pool of initially discarded samples (n = 20,750) (Extended Data Fig. 5, see Methods). Two-sample Kolmogorov-Smirnov tests comparing the metabolic distortion (differences between metabolic and chronological ages) revealed an exceptional structural alignment between the discarded samples and their matched reference counterparts.

To definitively confirm the robustness and generalizability of our interpretable model, we evaluated its predictive performance on an independent external control cohort from general population in Austria (n = 121, age range 18-89), a geographically unrelated area and whose samples were acquired and measured independently in a different laboratory. As shown in Fig. 2c, the regression of predicted metabolic age against chronological age in this external cohort (r = 0.81) closely mirrored that of an age-matched subset from our primary reference dataset (r = 0.89). Furthermore, Kolmogorov-Smirnov test distributions of both groups yielded a *p*-value of 0.1, statistically confirming that the model's behavior does not differ between populations.

Finally, to further assess the generalizability of the unified metabolic age model, we evaluated its performance separately in males and females and compared it with sex-specific models trained exclusively on each subgroup (Extended Data Fig. 6). The unified model achieved similarly strong accuracy in females (r = 0.909, RMSE = 8.3 years) and males (r = 0.850, RMSE = 9.0 years). Training sex-specific models did not yield substantial improvements: the female-only model performed nearly identically to the unified model (r = 0.908, RMSE = 8.2 years), and the male-only model showed just a modest increase in accuracy (r = 0.877, RMSE = 8.5 years). The slightly superior performance in females is likely explained by the larger number of older female participants in the dataset, reflecting their longer life expectancy.

Biological architecture of metabolic aging as revealed by SHAP analysis

To obtain a higher-level view of the biological processes underlying metabolic aging, SHAP values were grouped into predefined metabolic and clinical categories representing major physiological domains, including energy metabolism, kidney function, nitrogen homeostasis, inflammation, and cardiovascular risk markers

(Extended Data Table 22). This SHAP-group analysis revealed a clear and reproducible structure in the model's decision-making (Fig. 3).

The grouped SHAP analysis identifies chronic inflammation as the dominant axis of metabolic aging in this model, followed by nitrogen homeostasis, energy metabolism and structural integrity and systemic frailty. At the individual-feature level, albumin and erythrocyte sedimentation rate (ESR) displayed the largest mean absolute SHAP values (3.1 and 2.4 years, respectively), almost doubling the contribution of the next most influential features, alanine (Ala, 1.6 years) and 1,5-anhydrosorbitol (AnHsorb, 1.4 years).

It is well-known that sex is a key determinant for metabolism. Consequently, SHAP analyses also revealed clear sex-specific differences in the biochemical determinants of metabolic age. Importantly, these differences were reproducible both when male and female samples were analyzed within the unified model and when SHAP values were derived from the sex-specific models themselves (Extended Data Fig. 6). In females, urea and estimated glomerular filtration rate (eGFR) contributed more strongly to age prediction, whereas in males, Ala and AnHsorb ranked among the most influential features. Despite these sex-dependent differences, the dominant contributors to metabolic aging remained consistent across analyses: albumin and ESR emerged as the top predictors in both sexes and in both modeling strategies.

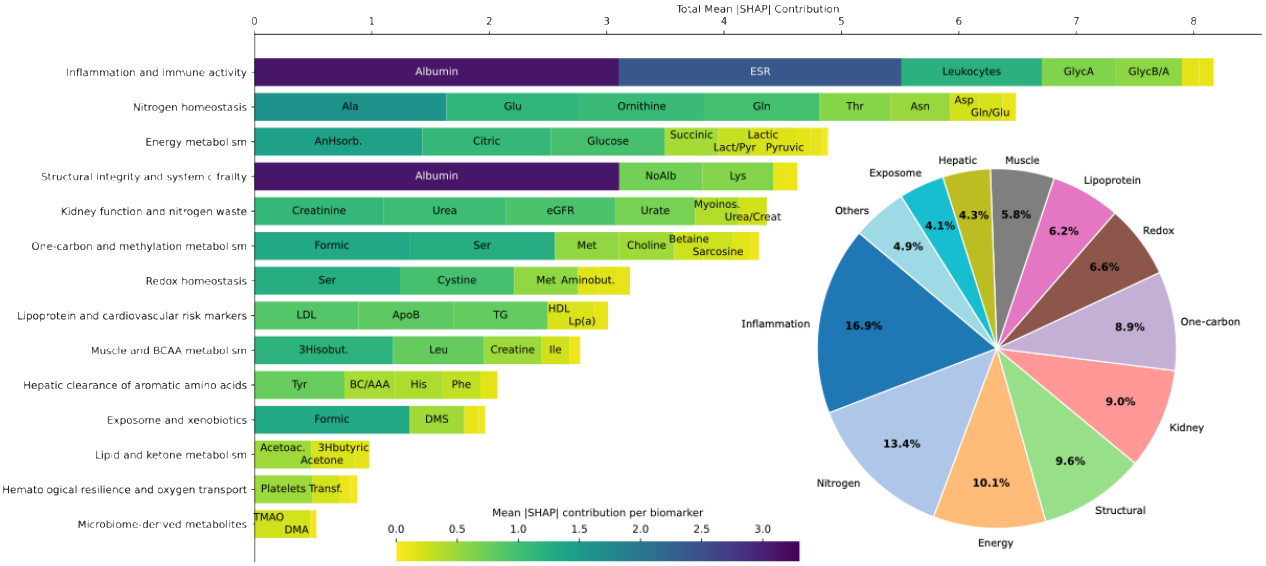

Fig. 3 | Contribution of SHAP groups. The main plot displays the total SHAP magnitude aggregated by predefined biological or clinical groups. An inset pie chart below illustrates the relative percentage contribution of each group to the overall metabolic age prediction. A complete list of the abbreviations used in this figure is available in the Supplementary Information (SupAbb.pdf).

Application of the metabolic age model to disease cohorts

We next investigated how the general population model behaves across a range of disease cohorts. Diseases included acute infections as well as non-communicable diseases and covering the main axis of pathology: cardiometabolic disease (CVD, MetS, CKD, MASLD), cancer (PRC), immunological disorders (IBD, PSO), neurodegenerative disease (ALS) and infection or infection-derived syndromes (COV, LCOV and FLU). For each condition, metabolic age was compared against chronological age, and the deviation from the reference regression line (termed metabolic distortion) was quantified. Positive distortion reflects an older-than-expected metabolic profile (accelerated aging), whereas negative distortion indicates relatively preserved or "younger" metabolic signatures.

To benchmark disease-associated deviations, each cohort was compared against a reference group of individuals from the general population matched by age. For both cases and references, we computed the distribution of metabolic distortion and represented it as histograms (Fig. 4a-k). As expected from the calibration of the model in the balanced population, the matched reference groups showed distortion distributions centered around zero. In contrast, all disease cohorts exhibited right-shifted distributions, indicative of accelerated metabolic aging, and increased dispersion, reflecting enhanced inter-individual heterogeneity. All case–reference comparisons were statistically significant according to the Kolmogorov–Smirnov test, with p-values far below 10^{-5} in most cohorts and $p = 0.001$ for LCOV. To further validate these

findings, the same procedure was applied to two control groups: an internal control consisting of the model's independent test set (ITCL, Fig. 4l), and the external control comprising the general population cohort from Austria (ETCL, Fig. 4m). Both groups yielded distributions that were not statistically distinguishable from the reference baseline, with Kolmogorov–Smirnov p-values of 0.2 and 0.1 for the internal and external controls, respectively. These results confirm that the observed metabolic shifts are disease-specific and robust to inter-laboratory variability.

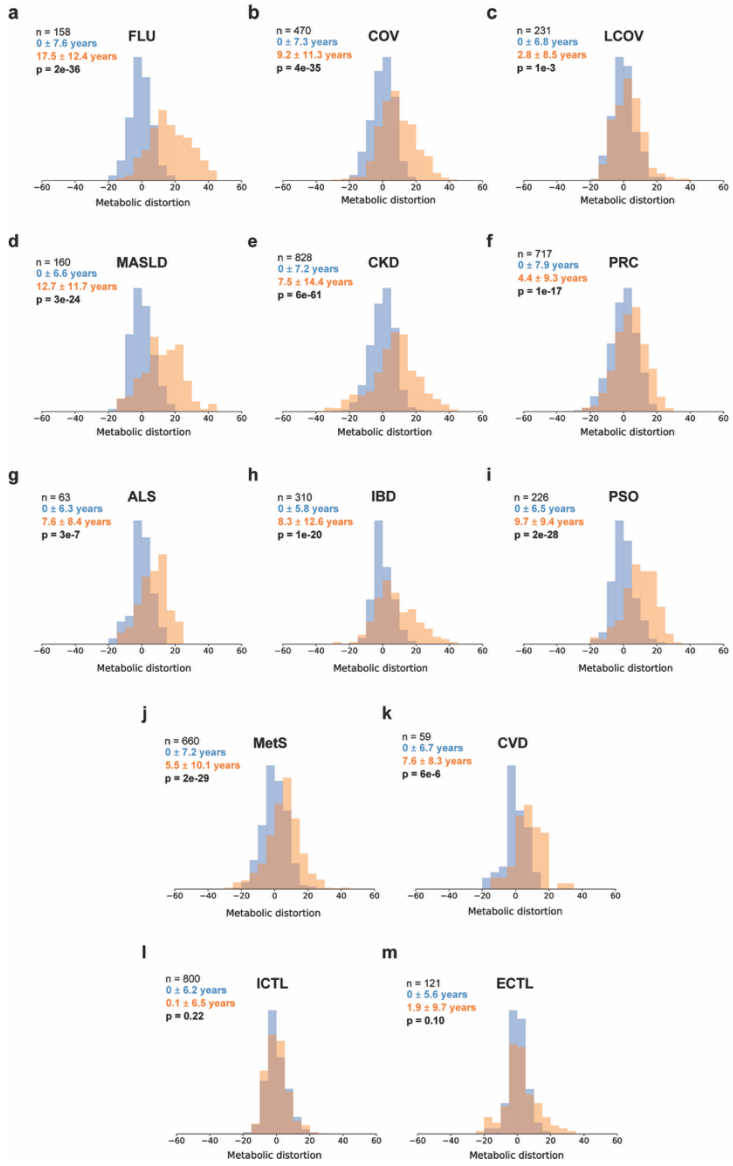

Fig. 4 | Metabolic distortion and SHAP differences across disease cohorts. a-k, Histograms of metabolic distortion (deviation from the reference regression line of metabolic age vs. chronological age) for each disease cohort (orange) and its age-matched reference group (blue), which was additionally sex-matched for the PRC cohort. For each panel, the sample size (n), the mean ± standard deviation of metabolic distortion for both groups, and the corresponding p-values from the Kolmogorov-Smirnov (K-S) test are indicated. **i-m,** Distribution of metabolic distortion for the internal control (independent model test set) and the external validation cohort (Austria), respectively, showing their alignment with the reference baseline.

To explore the reversibility of disease-driven metabolic aging, we investigated the IBD cohort by comparing patients in clinical remission against those with active disease (Extended Data Fig. 7). Patients in remission showed a metabolic distortion approximately 3 years lower than those in the active group, accompanied by a 3-year reduction in the standard deviation. This decreased variability was primarily driven by a lower prevalence of individuals with extreme metabolic age acceleration. These findings suggest that the metabolic distortion captured by our model is not a fixed state but can partially shift back toward the reference aging trajectory following clinical recovery (allostasis).

The prospective cardiovascular cohort is of particular interest in our analysis. Considering that all patients in this group experienced a CVD episode, examining their individualized metabolic age profiles is highly informative. The corresponding SHAP waterfall plots illustrating these individual trajectories are presented in Extended Data Fig. 8. Overall, the patterns are highly heterogeneous, underscoring the intrinsic complexity of individuals at the metabolic level and highlighting the multifactorial nature of CVD events. Most patients exhibited an increased metabolic age compared with their chronological age, although with diverse combinations of SHAP values, often consistent with pronounced lipid dysregulation, elevated glucose levels, and other CVD-associated markers. Interestingly, a common feature was elevated eGFR, which contributed to a lower predicted age (negative SHAP delta), likely reflecting a state of glomerular hyperfiltration; an early maladaptive hemodynamic response that often precedes cardiovascular events[28].

Representation of diseases along the metabolic aging trajectory

To investigate how the different diseases under consideration differ from the normal aging we have performed a PCA analysis of all the groups, specifically centering the analysis on the general population (Fig. 5a). As expected, the closest group to the age model is the Austrian external validation cohort (Fig. 5a, inset). In the opposite end falls the CKD cohort, consistent with the severity of the disease of patients bound to dialysis for survival. In the kidney disease cohort, while uremic toxins (urea, myo-inositol, urate) strongly pushed the metabolic age upward (Fig. 5b), creatinine exhibited a large negative SHAP difference (note that this refers to the feature's SHAP value impact on the model, not its raw clinical value), effectively acting as a "rejuvenating" factor. This occurs because, in the healthy training population, higher creatinine is a marker of preserved muscle mass and robustness. The model, unaware of the renal failure context, interprets the pathological retention of creatinine as a sign of muscular health[29].

Other diseases that are well discriminated by the aging model include MASLD and infectious diseases (FLU and COV). MASLD profoundly disrupts liver metabolism (the liver being the central metabolic organ) likely affecting serum homeostatic concentrations. In contrast, infections such as COV are known to induce a significant, albeit temporary, metabolically accelerated aging[30]. The remaining diseases show moderate acceleration, consistent with the idea that their main contributing factors are already embedded within the aging process. For example, IBD and PSO are largely driven by inflammatory markers similar to those observed in age-related inflammation (inflammaging), while aging and MetS are often difficult to distinguish, likely reflecting the influence of Western dietary and lifestyle patterns in the cohort used to develop the metabolic clock.

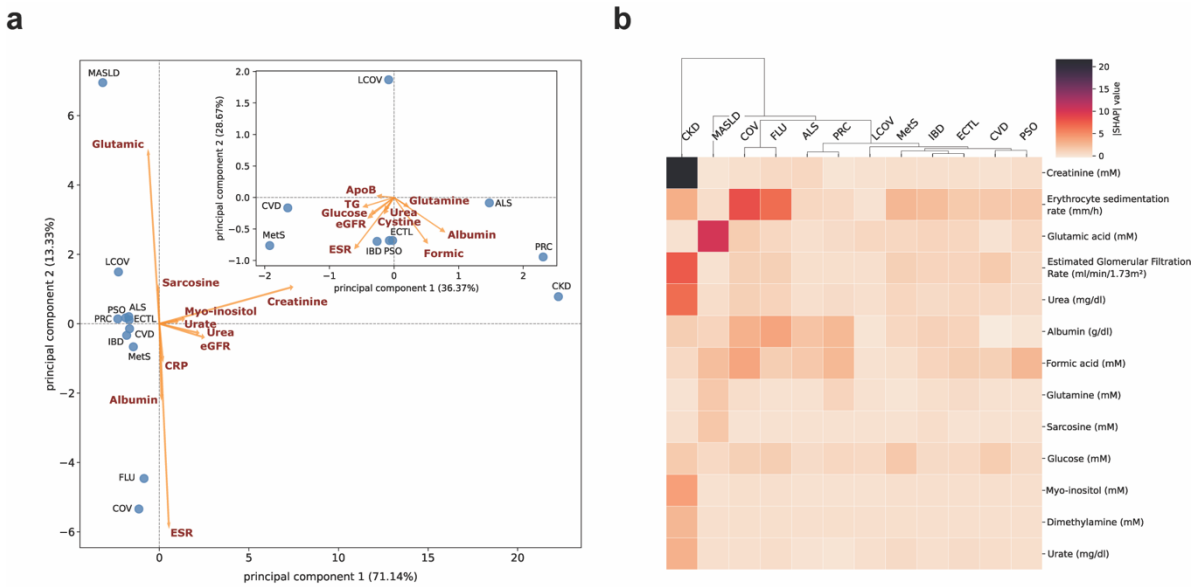

Fig. 5 | Principal component analysis and hierarchical clustering of disease cohorts based on metabolic age SHAP values. a, Principal component analysis (PCA) biplot displaying the metabolic aging signatures of all evaluated disease cohorts relative to the baseline healthy control state (centered at the origin). The analysis is entirely driven by the absolute SHAP (|SHAP|) values extracted from the general population metabolic age model. The loading vectors (arrows) indicate the top 10 most influential metabolites driving the variance across diseases. **Inset:** A focused PCA excluding the highly dispersed cohorts (CKD, MASLD, COV and FLU) to resolve the spatial distribution and metabolic similarities of the remaining tightly clustered diseases. **b,** Heatmap and hierarchical clustering of the

disease cohorts based on their feature importance profiles. Only metabolites or clinical variables with a substantial impact (|SHAP| value > 1.5) in at least one cohort are represented. The dendrogram groups the diseases using Ward's minimum variance method, revealing shared patterns of metabolic deviation from the healthy baseline. Color intensity corresponds to the magnitude of the SHAP values.

Discussion

The present study demonstrates that high-throughput serum NMR dataset analysis, combined with machine-learning modeling, yields a robust and biologically interpretable metabolic aging clock that captures disease-related deviations from healthy aging trajectories. Unlike previous studies, which often adjust for sex as a covariate or necessitate separate sex-specific clocks due to known dimorphisms in metabolic aging[31,32], we found that a single, unified model trained jointly on men and women performed as well as stratified versions. It is important to emphasize that this unification does not obscure biological nuances and, for example, markers of kidney function (urea, eGFR) contributed more strongly to the age estimate in women, whereas glycemic markers (Ala, AnHsor) were relatively more important in men, consistent with established sex differences in renal aging and glucose handling[33,34].

It is well-known that high-dimensional omics data often obscure single-feature explanations[35–37]. To overcome this effect, we implemented a framework based on quantified metabolites and clinical parameters obtained from the NMR data. This strategy yielded numerically stable and physiologically consistent SHAP patterns with only a modest trade-off in predictive performance, in line with previous observations where pathway-level features facilitated mechanistic insight without sacrificing robustness[37,38].

The principal marker related to aging is the inflammation and immune activity axis with the specific selection of albumin and ESR by the model over more transient markers like C-reactive protein. While cytokines and acute-phase proteins fluctuate rapidly, albumin (a negative acute-phase reactant) and ESR (driven by fibrinogen and immunoglobulins) provide a time-integrated readout of the systemic inflammatory state[39–41]. Glyc and SPC signals (uniquely measured by NMR spectroscopy) are well-known to be involved in acute inflammation[42,43] and they did moderately contribute to the age-related inflammation marker. All this fits neatly within the concept of "inflammaging," the chronic, low-grade, sterile inflammation that accumulates with age. Inflammaging is now recognized as a central mechanistic axis linking many of the hallmarks of aging to age-related diseases[44]. Moreover, the inflammatory burden seems to disrupt systemic energy homeostasis, generating a self-reinforcing cycle of immunometabolic dysregulation. The prominence of nitrogen homeostasis alongside energy metabolism indicates that alterations in systemic amino acid handling may be as critical as direct glycemic dysregulation in the aging process[45–47]. Closely linked to these shifts, structural integrity and systemic frailty emerged as a major determinant of the clock, largely driven by albumin levels. This reflects the dual nature of albumin in the context of aging: acting both as a negative acute-phase reactant linked to systemic inflammaging and as a fundamental indicator of nutritional status and protein reserve[1,48].

The metabolic clock also identifies kidney function and nitrogen waste as critical determinants of metabolic age. This relationship is consistent with recent evidence positioning the kidney as a paradigmatic organ of age-related decline, where the senescence-associated secretory phenotype and chronic inflammaging accelerate tissue dysfunction and impair regenerative capacity[49]. The combined SHAP contribution of urea, urate, and eGFR suggests that the model captures the progressive accumulation of uremic retention solutes and the gradual loss of filtration capacity associated with these processes. Furthermore, the interplay between one-carbon and methylation metabolism and redox homeostasis underscores the systemic impact of aging on cellular maintenance. The contribution of methylation-related metabolites and glutathione-precursor amino acids likely reflects the convergence of epigenetic drift and the gradual exhaustion of antioxidant defenses under persistent oxidative stress.

Finally, the persistence of an atherogenic profile within lipoprotein and cardiovascular risk markers, alongside alterations in muscle and BCAA metabolism, probably acts as a downstream integrator of this systemic deterioration. Heavily influenced by the dominant overall contribution of inflammation and immune activity, this signature suggests that cytokine-mediated disruption of proteostasis and systemic insulin resistance synergistically promote both atherogenic dyslipidemia and the metabolic signatures of muscle frailty.

The application of the model to disease cohorts revealed that "metabolic age acceleration" is not a uniform phenomenon but rather a disease-specific distortion of the healthy aging trajectory. We quantified this as the difference in SHAP values between patients and age-matched controls (Fig. 4 and Extended Data Fig. 9 and 10). The most profound distortions were observed in acute infections and active inflammatory states. Patients

with FLU, COV, and IBD exhibited large positive shifts in metabolic age driven by a massive intensification of the inflammatory axis. In these cohorts, the contributions of ESR, C-reactive protein, and albumin deviated dramatically from the reference (e.g., ESR SHAP delta > +5 years in FLU). This surge highlights that the "inflammaging" clock, when exposed to acute-phase responses, captures a biochemical mimicry of advanced catabolic aging[50]. Interestingly, LCOV presented a distinct signature with the overwhelming inflammatory signal subsided, and the drivers shifted toward metabolic inefficiencies, specifically glutamic acid and glucose. This suggests that persistent post-acute sequelae may be driven less by systemic inflammation and more by lingering dysregulation in bioenergetics and neurotransmitter metabolism[51].

MASLD exhibited a unique hierarchical reordering of metabolic drivers. Although inflammatory markers remained relevant, the primary driver of age acceleration was glutamic acid, which exhibited a massive positive SHAP contribution, clearly distinct from other cohorts. Glutamic acid occupies a central metabolic node, linking amino acid metabolism, the TCA cycle, nitrogen handling and the urea cycle, and glutathione synthesis. Although not specific to liver disease and reflective of systemic metabolic dysfunction, elevated glutamic acid in MASLD likely arises from increased protein turnover and amino flux, enhanced transamination reactions (e.g., ALT and AST), mitochondrial dysfunction, oxidative stress, and insulin resistance, which shifts central carbon metabolism toward amino acid-derived gluconeogenesis. Together, these processes lead to altered glutamic acid handling and its accumulation in circulation[52]. Similarly, in the CKD cohort, the model captured a pronounced organ-specific metabolic rewiring. The overall metabolic distortion was heavily dominated by the systemic accumulation of uremic toxins (including urea, myo-inositol, and urate) and major alterations in creatinine levels, which collectively emerged as the principal drivers of metabolic age prediction, reflecting the profound consequences of declining renal filtration capacity.

In line with these observations, PCA analysis across the cohorts delineated three clear axes of metabolic distortion (Fig. 5). One major axis reflects renal impairment, heavily weighted by eGFR and diverse uremic toxins. A second axis maps the inflammatory burden, driven by albumin, ESR, and C-reactive protein, which clearly isolates the infectious disease cohorts (COV and FLU). The third axis captures a strictly metabolic signature, primarily governed by glutamic acid and sarcosine, which distinctly characterizes the MASLD cohort. This spatial separation further illustrates how different diseases accelerate the metabolic clock through independent, biologically coherent pathways.

A clinically relevant finding emerged from the prospective CVD cohort. Although clinically healthy at baseline, individuals who subsequently developed cardiovascular events exhibited a distinct metabolic acceleration of approximately 8 years relative to matched controls. This anticipatory shift suggests that the model captures subtle, prodromal biochemical alterations well before the onset of overt clinical symptoms.

The study has several limitations. Although the cohort is large and age-balanced, it predominantly represents a Caucasian population. Furthermore, the paradox of "false rejuvenators" remains a conceptual challenge at the individual feature level. This phenomenon occurs because certain parameters reflect different physiological states in normal aging compared to specific diseases. For example, while elevated creatinine is a sign of pre-served muscle mass and robustness in the healthy general population, it is a marker of severe renal damage in patients with CKD. Such context-dependent reversals can theoretically mislead models into assigning a lower biological age to sick individuals, as has been previously observed in predictive clocks applied to colorectal cancer patients[53]. Therefore, the specific variables driving metabolic deviations must always be interpreted independently within a clinical framework, as a "younger" molecular signal is not inherently beneficial if it stems from a disruption of normal homeostasis. That said, although individual features could exhibit isolated "rejuvenating" SHAP values in our study, this effect was consistently outweighed by the broad coverage of our biomarker panel across diverse physiological processes, and our interpretable model never produced a net deviation toward a younger overall metabolic age in any of the analyzed disease cohorts.

In conclusion, this work establishes an interpretable and scalable NMR-based metabolic aging clock that captures both the shared and disease-specific biochemical processes underlying human aging. By integrating metabolite quantification with clinically relevant biomarkers and addressing multicollinearity through a biologically informed framework, the model achieves a balance between predictive performance and mechanistic insight. Beyond accurate age estimation, the concept of metabolic distortion provides a useful tool to understand how different pathologies diverge from normative aging trajectories, highlighting the heterogeneity of disease-associated metabolic remodeling. Future studies should focus on extending validation across more diverse populations, incorporating longitudinal data to capture temporal dynamics, and integrating additional omics layers to further refine the biological interpretation of metabolic aging.

Methods

Cohorts and study population. This study incorporated data from a multi-national consortium. The reference population was recruited across Spain and Portugal, whereas independent disease cohorts were collected from Spain, Italy and the United Kingdom. Additionally, a general population control cohort from Austria was included for external validation of the reference population model. All samples were double coded prior to analysis to ensure full anonymization. The cohorts included in the foundational dataset are described in the corresponding supplementary file (SupCoDe.pdf), with detailed metadata and descriptive statistics for each cohort provided in Extended Data Tables 1-20.

Blood collection and serum preparation. Venous blood was obtained from fasting individuals (unless otherwise specified) following standardized operating procedures, as previously described[54]. After allowing coagulation at room temperature, samples were centrifuged, and the serum was aliquoted into cryogenic vials. All aliquots were stored at –80 °C until analysis, to ensure sample stability and comparability across cohorts. The protocol was implemented uniformly across all participating centers to minimize pre-analytical variability.

NMR spectra acquisition. High-throughput ^{1}H-NMR spectra were acquired on Bruker Avance III HD and Neo 600 MHz instruments equipped with BBI or TXI probes and SampleJet™ automation systems. Measurements were performed at 310K following previously validated calibration and QC procedures to secure reproducibility[27]. For each serum sample, three spectral datasets were generated: (i) a quantitative 1D ^{1}H NOESY experiment with water suppression (Bruker pulse program *noesygppr1d*), (ii) a 1D CPMG (Carr–Purcell–Meiboom–Gill) sequence (*cpmgpr1d*), used to attenuate signals from macromolecules such as proteins and lipoproteins and single out low-molecular-weight metabolites, and (iii) a fast 2D J-resolved experiment (J-Res, *jrespprqf*), to resolve peak overlap, assist in metabolite assignment and improve quantification. The automated Bruker metabolite and lipoprotein profiles used for comparison were generated automatically from these spectra using B.I.Quant-PS™ and B.I.LISA™ software respectively. Additionally, 1D-PGPE (Pulsed Gradient Perfect Echo, *zggppezf.ivdr*) spectra were acquired to quantify specific inflammation markers (GlycA, GlycB, and SPC) using Bruker algorithms (PhenoRisk PACS^{TM})[55].

Data preprocessing. Intensity normalization was performed using the electronic reference signal for in-tube calibration (ERETIC) method, which introduces an artificial reference signal in each spectrum with an integral corresponding to a 10 mM ^{1}H concentration. Subsequently, chemical-shift alignment was refined by calibrating each spectrum to the alanine CH_3 resonance, ensuring that peak positions were harmonized across the dataset. To guarantee that all spectra shared an identical chemical-shift grid, each spectrum was interpolated to a common ppm axis prior to feature extraction. After alignment, a spectral binning optimization procedure was carried out to determine the best trade-off between dimensionality reduction and information retention. For the age model, a final bin width of 0.0115 ppm (n = 1,039 points) was selected, corresponding to a 50-fold reduction of the processed spectral resolution (Extended Data Fig. 12). All NMR data for the clinical-parameter prediction models was preprocessed using an analogous bin optimization strategy.

For alternative modelling based on raw time-domain NMR data, the FID was used directly as input instead of the processed spectrum. As an analogue to spectral binning, each FID was truncated after 512 complex points (with 512 real and 512 imaginary components), corresponding to the high–signal-to-noise region of the acquisition and capturing most of the informative time-domain dynamics. No additional apodization or zero-filling was applied, thus minimizing any bias and allowing the model to learn directly from the intrinsic FID structure.

Metabolite quantification. To resolve overlapping resonances and obtain clear signals for complex metabolites, we utilized two-dimensional J-resolved (J-res) spectroscopy. However, because J-res is inherently non-quantitative, targeted spiking experiments were required to extract specific calibration coefficients. These coefficients were subsequently incorporated into a quantitative pipeline applied to the J-res spectra to calculate the final concentrations for up to 49 metabolites. Conversely, for metabolites exhibiting well-resolved, non-overlapping resonances directly in the 1D NOESY spectra, concentrations were derived from the standard Bruker quantitative profiling (B.I.Quant-PS^{TM})[22]. This combined strategy allowed us to optimize precision and robustness across metabolites with different spectral characteristics. As metabolite levels were used as model features, the procedure prioritized internal precision and cross-sample consistency over absolute quantification. The quantified metabolites are listed in Extended Data Table 21.

In addition, special care was taken to resolve specific peak overlaps for trimethylamine-N-oxide (TMAO) and sarcosine. TMAO and betaine share a major resonance at approximately 3.28 ppm, which is the only detectable signal for TMAO, but one of several for betaine. To disentangle their contributions, betaine was first quantified from its well resolved resonance at ~3.91 ppm; its expected contribution to the signal integral at 3.28 ppm was then back-calculated and subtracted to derive the TMAO concentration from the residual signal integral. Sarcosine shows an intense singlet at 2.76 ppm from its CH_3 group that overlaps with the triplet signal from an aliphatic fatty acid. Considering the expected 1:2:1 intensity distribution within a triplet then allowed to extrapolate its overlapping central from one well resolved lateral signal integral and subtracting the former to derive the sarcosine concentration from the residual integral.

Prediction of clinical parameters. Concomitant with metabolite quantification, we derived a complementary set of 25 clinical biomarkers directly from the quantitative 1D ^{1}H spectra using supervised regression models. These were trained to reproduce standard laboratory measurements alongside Bruker-derived quantifications for GlycA, GlycB, and SPC. Pipeline selection and hyperparameter optimization were carried out using the TPOT AutoML framework[56]. Each model was evaluated by computing the Pearson correlation between NMR estimated values and their corresponding clinical measurements on an independent 20% test subset excluded from the model training. The full list of inferred biomarkers is given in Extended Data Table 21.

Balancing strategy. From a total initial dataset of 29,390 samples from the general population, and to avoid age related sampling biases, the dataset was stratified into five age intervals (7–30, 31–40, 41–50, 51–65, and >65 years). To ensure balanced representation across both age and sex (total n = 8,640), an equal number of participants was randomly selected from the first three intervals. For the oldest category, where women are naturally more represented due to higher life expectancy, the sampling was adjusted to ensure the overall sex balance across the entire dataset. This led to a compensatory imbalance within the older groups, where the smaller number of male participants selected in the >65 age group (735) was offset by selecting a correspondingly larger number of male participants in the 51-65 age group (993), as summarized in Extended Data Table 23. Extended Data Fig. 13 compares the age distribution of the full dataset with that of the balanced subset.

Machine learning models for age prediction. All models were trained using an identical machine learning architecture derived from the TPOT AutoML framework. After feature standardization, predictions were generated through a stacking ensemble combining a Ridge linear regression[57] model with an ExtraTrees regressor[58]. For each modeling strategy, the dataset was partitioned such that 20% of the samples were excluded from the training to lateron serve as an independent test set for final evaluation. The remaining 80% of the data was used for training and internal validation through five-fold cross-validation.

For the iterative negative control approach (Extended Data Fig. 5), a pool of initially discarded samples (n = 20,750) was used in 1,000 iterations of 1,000 healthy discarded samples each. For each iteration, a new specific sub-cohort from the reference data was dynamically drawn to precisely match the age distribution of the discarded subset, and their metabolic distortions were computed. Two-sample Kolmogorov-Smirnov tests revealed an exceptional structural alignment between the discarded samples and their matched reference counterparts, as characterized by an insignificantly small mean D-statistic (Extended Data Fig. 5b) and a vast majority of non-significant iterations (Extended Data Fig. 5c).

Model interpretability. Feature relevance and model behavior were analyzed using SHAP explanations[59]. To obtain a stable and biologically meaningful interpretation focused on the magnitude of influence, individual SHAP values were aggregated into predefined SHAP groups corresponding to specific metabolic pathways and clinical domains (Extended Data Table 22). The SHAP value for each group was calculated as the sum of the absolute SHAP values of all its constituent features.

Software and computational environment. All data processing, automated machine learning, and statistical analyses were implemented in Python (v. 3.9.17). The core computational environment utilized NumPy (v. 1.23.5) and Pandas (v. 1.5.3) for data manipulation, nmrglue (v. 0.9) for NMR data extraction and processing, scikit-learn (v. 1.4.1.post1) and TPOT (v. 0.12.2) for machine learning workflows, SHAP (v. 0.42.1) for model interpretation, and Matplotlib (v. 3.7.2) for data visualization. To guarantee strict cross-platform reproducibility, the complete analytical pipelines for both metabolite quantification and the prediction of clinical parameters were encapsulated within a custom Docker container based on a lightweight Debian environment.

Data availability

Underlying data are available upon reasonable request to the corresponding authors, subject to cohort-specific data-sharing agreements and ethical restrictions.

References

1. López-Otín, C., Blasco, M. A., Partridge, L., Serrano, M. & Kroemer, G. The hallmarks of aging. *Cell* vol. 153 Preprint at https://doi.org/10.1016/j.cell.2013.05.039 (2013).
2. Ferrucci, L. *et al.* Measuring biological aging in humans: A quest. *Aging Cell* **19**, 1–21 (2020).
3. Robinson, O. & Lau, C. E. www.aging-us.com AGING 2020, Vol. 12, No. 22. *Aging* **12**, 22352–22353 (2020).
4. Hertel, J. *et al.* Measuring Biological Age via Metabonomics: The Metabolic Age Score. *J. Proteome Res.* **15**, 400–410 (2016).
5. López-Otín, C., Blasco, M. A., Partridge, L., Serrano, M. & Kroemer, G. Hallmarks of aging: An expanding universe. *Cell* **186**, 243–278 (2023).
6. Hannum, G. *et al.* Genome-wide Methylation Profiles Reveal Quantitative Views of Human Aging Rates. *Mol. Cell* **49**, 359–367 (2013).
7. Fischer, K. *et al.* Biomarker Profiling by Nuclear Magnetic Resonance Spectroscopy for the Prediction of All-Cause Mortality: An Observational Study of 17,345 Persons. *PLoS Med.* **11**, (2014).
8. Deelen, J. *et al.* A metabolic profile of all-cause mortality risk identified in an observational study of 44,168 individuals. *Nat. Commun.* **10**, (2019).
9. Johnson, A. A., Shokhirev, M. N., Wyss-Coray, T. & Lehallier, B. Systematic review and analysis of human proteomics aging studies unveils a novel proteomic aging clock and identifies key processes that change with age. *Ageing Research Reviews* vol. 60 Preprint at https://doi.org/10.1016/j.arr.2020.101070 (2020).
10. López-Otín, C., Galluzzi, L., Freije, J. M. P., Madeo, F. & Kroemer, G. Metabolic Control of Longevity. *Cell* **166**, 802–821 (2016).
11. Gil-Redondo, R. *et al.* MetSCORE: a molecular metric to evaluate the risk of metabolic syndrome based on serum NMR metabolomics. *Cardiovasc. Diabetol.* **23**, (2024).
12. Hertel, J. *et al.* Measuring Biological Age via Metabonomics: The Metabolic Age Score. *J. Proteome Res.* **15**, 400–410 (2016).
13. Van Den Akker, E. B. *et al.* Metabolic age based on the BBMRI-NL 1H-NMR metabolomics repository as biomarker of age-related disease. *Circ. Genom. Precis. Med.* 541–547 (2020) doi:10.1161/CIRCGEN.119.002610.
14. Zhang, S. *et al.* A metabolomic profile of biological aging in 250,341 individuals from the UK Biobank. *Nat. Commun.* **15**, 8081 (2024).
15. Mutz, J., Iniesta, R. & Lewis, C. M. Metabolomic age (MileAge) predicts health and life span: A comparison of multiple machine learning algorithms. *Sci. Adv.* **10**, (2024).
16. Shang, X. *et al.* Metabolomic age and risk of 50 chronic diseases in community-dwelling adults: A prospective cohort study. *Aging Cell* **23**, (2024).
17. Soininen, P., Kangas, A. J., Würtz, P., Suna, T. & Ala-Korpela, M. Quantitative serum nuclear magnetic resonance metabolomics in cardiovascular epidemiology and genetics. *Circ. Cardiovasc. Genet.* **8**, 192–206 (2015).
18. Bragg, F. *et al.* Predictive value of circulating NMR metabolic biomarkers for type 2 diabetes risk in the UK Biobank study. *BMC Med.* **20**, 159 (2022).

19. Klén, R. *et al.* Predicting skeletal muscle and whole-body insulin sensitivity using NMR-metabolomic profiling. *J. Endocr. Soc.* **4**, 1–18 (2020).

20. Ibáñez de Opakua, A. *et al.* Metabolomic-based aging clocks. *NPJ Metabolic Health and Disease* **3**, 1–6 (2025).

21. Vignoli, A., Cacciatore, S. & Tenori, L. Deriving three one dimensional NMR spectra from a single experiment through machine learning. *Nature Communications* **16**, 1–13 (2025).

22. Belsley, D. A., Kuh, E. & Welsch, R. E. *Regression Diagnostics: Identifying Influential Data and Sources of Collinearity*. (John Wiley & Sons, Ltd, 1980).

23. Martin-Ramos, S. *et al.* Enhanced Standard Operating Procedures for 31P NMR-Based Metabolomics in Tissue Extracts. *JACS Au* (2025).

24. Würtz, P. *et al.* Quantitative Serum Nuclear Magnetic Resonance Metabolomics in Large-Scale Epidemiology: A Primer on -Omic Technologies. *Am. J. Epidemiol.* **186**, 1084–1096 (2017).

25. Giraudeau, P. Quantitative NMR spectroscopy of complex mixtures. *Chemical Communications* **59**, 6627–6642 (2023).

26. Jiménez, B. *et al.* Quantitative Lipoprotein Subclass and Low Molecular Weight Metabolite Analysis in Human Serum and Plasma by (1)H NMR Spectroscopy in a Multilaboratory Trial. *Anal Chem* **90**, 11962–11971 (2018).

27. Loo, R. L. *et al.* Quantitative In-Vitro Diagnostic NMR Spectroscopy for Lipoprotein and Metabolite Measurements in Plasma and Serum: Recommendations for Analytical Artifact Minimization with Special Reference to COVID-19/SARS-CoV-2 Samples. *J. Proteome Res.* **19**, 4428–4441 (2020).

28. Kim, J. S. *et al.* Renal hyperfiltration as risk factor of major adverse cardiovascular events in patients with acute myocardial infarction. *Sci. Rep.* **15**, 1–9 (2025).

29. Agudelo-Botero, M., Sharashkina, N., Liu, X. & Liu, C. *Sarcopenia Index Based on Serum Creatinine and Cystatin C Is Associated with Mortality in Middle-Aged and Older Adults in Chinese: A Retrospective Cohort Study from the China Health and Retirement Longitudinal Study*.

30. Bruzzone, C., Conde, R., Embade, N., Mato, J. M. & Millet, O. Metabolomics as a powerful tool for diagnostic, pronostic and drug intervention analysis in COVID-19. *Frontiers in Molecular Biosciences* vol. 10 Preprint at https://doi.org/10.3389/fmolb.2023.1111482 (2023).

31. Ibáñez-Cabellos, J. S., Sandoval, J., Pallardó, F. V., García-Giménez, J. L. & Mena-Molla, S. A Sex-Specific Minimal CpG-Based Model for Biological Aging Using ELOVL2 Methylation Analysis. *Int. J. Mol. Sci.* **26**, 3392 (2025).

32. Peng, L., Xie, R., Holleczek, B., Brenner, H. & Schöttker, B. Development of Age- and Sex-Specific Metabolomics-Based Biological Ageing Clocks for 10-Year Mortality Prediction. *Advanced Science* **13**, 1–20 (2026).

33. Harvey, B. J. & Alvarez de la Rosa, D. Sex Differences in Kidney Health and Disease. *Nephron* **149**, 1–27 (2024).

34. Lodge, S. *et al.* NMR spectroscopy derived plasma biomarkers of inflammation in human populations: Influences of age, sex and adiposity. *PLoS One* **20**, e0311975 (2025).

35. Ji, Q. *et al.* Multimodal Omics Approaches to Aging and Age-Related Diseases. *Phenomics* **4**, 56–71 (2024).

36. Huang, H. *et al.* Decoding aging clocks: New insights from metabolomics. *Cell Metab.* **37**, 34–58 (2025).

37. Macdonald-Dunlop, E. *et al.* A catalogue of omics biological ageing clocks reveals substantial commonality and associations with disease risk. *Aging* **14**, 623–659 (2022).

38. Li, P. *et al.* Decoding disease–specific ageing mechanisms through pathway-level epigenetic clock: insights from multi-cohort validation. *EBioMedicine* **118**, 105829 (2025).

39. Fest, J. *et al.* Erythrocyte sedimentation rate as an independent prognostic marker for mortality: a prospective population-based cohort study. *J. Intern. Med.* **285**, 341–348 (2019).

40. Riviati, N. *et al.* Serum Albumin as Prognostic Marker for Older Adults in Hospital and Community Settings. *Gerontol. Geriatr. Med.* **10**, (2024).

41. Watson, J., Whiting, P., Salisbury, C., Banks, J. & Hamilton, W. Raised inflammatory markers as a predictor of one-year mortality: A cohort study in primary care in the UK using electronic health record data. *BMJ Open* **10**, 1–7 (2020).

42. Nitschke, P. *et al.* J-Edited DIffusional Proton Nuclear Magnetic Resonance Spectroscopic Measurement of Glycoprotein and Supramolecular Phospholipid Biomarkers of Inflammation in Human Serum. *Anal. Chem.* **94**, 1333–1341 (2022).

43. Bizkarguenaga, M. *et al.* Uneven metabolic and lipidomic profiles in recovered COVID-19 patients as investigated by plasma NMR metabolomics. *NMR Biomed.* **35**, e4637 (2022).

44. Franceschi, C., Garagnani, P., Parini, P., Giuliani, C. & Santoro, A. Inflammaging: a new immune–metabolic viewpoint for age-related diseases. *Nat. Rev. Endocrinol.* **14**, 576–590 (2018).

45. Xu, J., Zhou, H. & Wang, Z. Accelerated biological aging mediates the associations of stress hyperglycemia ratio (SHR) with mortality in type 2 diabetes and obesity (diabesity). *Cardiovasc. Diabetol.* **24**, 1–13 (2025).

46. Zhang, Z. *et al.* Accelerated biological aging, mediating amino acids, and risk of incident type 2 diabetes: a prospective cohort study. *J. Endocrinol. Invest.* **48**, 435–443 (2025).

47. Khalaf, F., Barayan, D., Saldanha, S. & Jeschke, M. G. Metabolaging: a new geroscience perspective linking aging pathologies and metabolic dysfunction. *Metabolism* **166**, 156158 (2025).

48. Wang, Z., Yu, S., Du, X., Yan, X. & Xin, Y. Role of branched chain amino acid metabolism on aging. *Biogerontology* **26**, 169 (2025).

49. Luca, F. De *et al.* From Senescent Cells to Systemic Inflammation: The Role of Inflammaging in Age-Related Diseases and Kidney Dysfunction. *Cells* **14**, 1–23 (2025).

50. Henry, B., Santos de Oliviera, M., Benoit, S., Plebani, M. & Lippi, G. Hematological, biochemical and immune biomarker abnormalitie associted with severe ilness and mortality in coronavirsu disease (COVID-19): meya-analysis. *Clin Chem Lab Med* **10**, 0–4 (2020).

51. Holmes, E; Wist, J; Masuda, R; Lodge, S; Nitschke, P; Kimhofer, T; Loo, RL; Begum, S; Boughton, B; Yang, R; Morillon, AC; Chin, ST; Hall, D; Ryan, M; Bong, SH; Gay, M; Hartmut Lawler, NG; Gray, N; Whiley, L; Nicholson, JK. Incomplete Systemic Recovery and Metabolic Phenoreversion in Post-Acute-Phase Nonhospitalized COVID-19 Patients: Implications for Assessment of Post-Acute COVID-19 Syndrome. *J. Proteome Res.* (2021).

52. Masoodi, M. *et al.* Metabolomics and lipidomics in NAFLD: biomarkers and non-invasive diagnostic tests. *Nat. Rev. Gastroenterol. Hepatol.* **18**, 835–856 (2021).

53. Zhang, L. *et al.* Global metabolomics revealed deviations from the metabolic aging clock in colorectal cancer patients. *Theranostics* **14**, 1602–1614 (2024).

54. Bizkarguenaga, M. *et al.* Prospective Metabolomic Studies in Precision Medicine: The AKRIBEA Project. in *Handbook of Experimental Pharmacology* vol. 277 275–297 (2022).

55. Lodge, S. *et al.* Diffusion and Relaxation Edited Proton NMR Spectroscopy of Plasma Reveals a High-Fidelity Supramolecular Biomarker Signature of SARS-CoV-2 Infection. *Cite This: Anal. Chem* **93**, 3976–3986 (2021).

56. Olson, R. S. & Moore, J. H. TPOT: A Tree-Based Pipeline Optimization Tool for Automating Machine Learning. in 151–160 (2019). doi:10.1007/978-3-030-05318-5_8.

57. Hoerl, A. E. & Kennard, R. W. Ridge Regression: Biased Estimation for Nonorthogonal Problems. *Technometrics* **12**, 55–67 (1970).

58. Geurts, P., Ernst, D. & Wehenkel, L. Extremely randomized trees. *Mach. Learn.* **63**, 3–42 (2006).

59. Lundberg, S. M., Allen, P. G. & Lee, S.-I. *A Unified Approach to Interpreting Model Predictions*. https://github.com/slundberg/shap.

Acknowledgements

We thank all cohort members and researchers who participated in this study, and especially the patients and the Biobank of the Aragon Health System (PT23/00146), integrated in the ISCIII Platform for Biobanks and Biomodels, for their collaboration. This work was supported by the Department of Economic Development and Infrastructures of the Basque Government (Elkartek bg2021, bg2023, bg2025) and the Plan Complementario en Biotecnología Aplicada en Salud. Funding was also provided by the European Research Council (ERC) under the European Union's Horizon Europe programme (grant agreement No. 101096251-CoDeFeL). We also acknowledge support from the Alexander von Humboldt Professorship, the Horizon Europe MSCA project ModConFlex (101073558), DFG Transregio 154, AFOSR (24IOE027), SURE-AI (Research Council of Norway, 357482), and the Madrid Government-UAM Excellence Programme (V PRICIT). We were also supported by MICIU (PID2024-160696OB-I00, PDC2025-165310-I00, PID2023-146872OB-I00-DyCMaMod). We thank the Center for Medical Research, Medical University of Graz, Graz, Austria for laboratory access. We are grateful to the Austrian Science Fund (FWF) for excellence cluster 10.55776/COE14, Grants DOI 10.55776/P28854, 10.55776/I3792, 10.55776/DOC130, and 10.55776/W1226, the Austrian Research Promotion Agency (FFG) grants 864690 and 870454; the Integrative Metabolism Research Center Graz; the Austrian Infrastructure Program 2016/2017; the Styrian Government (MetAGE, Zukunftsfonds, doc.fund program); the City of Graz (MetAGE, doc.fund); and BioTechMed-Graz (flagship project). This project was funded in part by the FFG and the European Union (EFRE) under grant 912192. We would like to express our sincere gratitude to all the representatives of the Research Unit of the Spanish Kidney Foundation and the Asociación Long COVID de Euskal Herria, who have participated in this work.

Author contributions

Conceptualization: AIdeO, UB, RM, LV, CL, EZ, JMM, and OM. Data curation: AIdeO, BG-V, RG-R, HH, CH, NV, BO-P, EA-A, SuM, AMS, GH, MB-M, JA-G, AS, NO, IV, MJZ-B, MRG-F, DF-B, TM, MU-U, ArC, AdC, RS-P, EB, QA, FM, LV, DC, HdlF, FC, DA, JP-G, MC, GG, and TB. Formal analysis: AIdeO, RG-R, HH, CH, NV, BO-P, and TM. Funding acquisition: AnC, UB, TM, NE, EZ, JMM, and OM. Investigation: AIdeO, MB, AdD, RC, BG-V, TS, MLS, AnC, VL, SaM, SP, HH, CH, NV, BO-P, MB-M, PJM-G, FS-T, JA-G, JIA, MI, MAM, XC, AG, GB-S, AS, NO, IV, MJZ-B, MRG-F, DF-B, LN-A, ML-V, UB, RM, MU-U, ArC, AdC, LT, RS-P, EB, QA, FM, LV, DC, HdlF, FC, DA, JP-G, MC, GG, and TB. Methodology: AIdeO, UB, RM, TD, HS, MS, CC, EZ, and OM. Project administration: JMM and OM. Resources: TM, HS, MS, CC, NE, and OM. Writing – original draft: AIdeO. Writing – review & editing: AIdeO, MB, AdD, RC, BG-V, RG-R, TS, MLS, AnC, VL, SaM, SP, HH, CH, NV, BO-P, MPS-F, EA-A, SuM, AMS, GH, MB-M, PJM-G, FS-T, JA-G, JIA, MI, MAM, XC, AG, GB-S, AS, NO, IV, MJZ-B, MRG-F, DF-B, LN-A, ML-V, UB, RM, TM, MU-U, ArC, TD, AdC, HS, MS, CC, LT, RS-P, EB, QA, NE, SCL, FM, LV, CL, DC, HdlF, FC, DA, JP-G, MC, GG, TB, EZ, JMM, and OM.

Competing interests

The authors declare no competing interests.

Additional information

Extended data for this paper is available in the ExtData.pdf file.

Supplementary information is available in the SupCoDe.pdf and SupAbb.pdf files.